

For submission to The Journal of Catalysis

**Ligand-Coordination Effects on the Selective Hydrogenation of Acetylene
in Single-site Pd-Ligand Supported Catalysts**

**Eman Wasim,^[a] Naseem Ud Din,^[b] Duy Le,^[b] Xuemei Zhou,^{[a],[d]} Michael S. Pape,^[c]
George E. Sterbinsky,^[c] Talat S. Rahman,^{[b],*} Steven L. Tait^{[a],*}**

^[a] E. Wasim, Dr. X. Zhou, Prof. S. L. Tait, Department of Chemistry, Indiana University, 800 E. Kirkwood Ave., Bloomington, Indiana 47405, USA.

* E-mail: tait@indiana.edu, Tel.: +1-812-855-1302.

^[b] Dr. N. U. Din, Dr. D. Le, Dr. T. S. Rahman, Department of Physics, University of Central Florida, Orlando, FL, USA.

*Email: Talat.Rahman@ucf.edu

^[c] Dr. G. E. Sterbinsky, M. S. Pape, Advanced Photon Source, Argonne National Laboratory, 9700 S. Cass Ave., Lemont, Illinois 60439, USA.

^[d] Present address: School of Chemical Engineering, Sichuan University, No. 24 South Section 1, Yihuan Road, Chengdu, 610065, P.R.C.

Abstract

The selective hydrogenation of acetylene to ethylene is a critical step in the synthesis of polyethylenes. Achieving high conversion to ethylene without over-hydrogenation to ethane is a challenge that requires control of the transition metal site, which we achieve through a ligand-coordinated supported catalyst (LCSC) strategy. Using Pd catalysts coordinated to 1,10-phenanthroline-5,6-dione (PDO) ligands on CeO₂ supports, we have discovered that the reaction selectivity depends strongly on the ligand:metal ratio with higher selectivity when more ligand is present in the catalyst. Catalyst structure was examined by extended X-ray absorption fine structure spectroscopy, transmission electron microscopy, and CO adsorption, which indicate single-atom character of the Pd. The ligand:metal ratio is determined by X-ray photoelectron spectroscopy measurements and correlated with hydrogenation reactions under steady-state flow conditions to examine trends in hydrogenation activity and selectivity. Those trends can be better understood by density functional theory calculations that indicate hydrogen binding on the ligand to guide reaction selectivity toward the desired ethylene hydrogenation product. These results demonstrate the importance of considering the dynamic character of LCSCs and inform the design of future single-site heterogeneous catalysts.

Keywords

Ligand Coordinated Single Site Catalysts; Pd Selective Hydrogenation of Acetylene; Density Functional Theory; Extended X-ray Absorption Fine Structure Spectroscopy; X-Ray Photoelectron Spectroscopy.

Introduction

Hydrogenation is one of the most important industrial catalytic reactions, particularly due to its importance in industrial reactions for a variety of uses including the synthesis of fine chemicals and pharmaceuticals and polymer production [1]. In a hydrogenation reaction, a double or triple carbon-carbon bond is reduced or saturated to give rise to carbon-hydrogen bonds. Typically, the hydrogenation reaction takes place in the presence of molecular hydrogen and transition metal based catalysts such as Ni, Pd, or Pt which can be supported (usually on metal oxide powders) [2-4] or unsupported in the form of isolated nanoparticles [5-8]. Selectivity of these catalysts plays an important role for industrial reactions that require only partial hydrogenation of alkynes to produce alkenes. For example, the selective hydrogenation of acetylene to produce ethylene is a critical step in the synthesis of various valuable polyethylenes, which are used as building blocks for polymers, vitamins, agrochemicals, and fragrances [9, 10].

Ethylene polymerization requires a negligible acetylene concentration in the feed-stream since even small traces of C_2H_2 and higher alkyne contaminant from the ethylene source have the potential to poison the catalysts being employed for polymerization [11, 12]. The alkene precursors being used for these reactions are the products of catalytic and steam cracking of naphtha or alkylation reactions. These reactions are highly unselective and produce many side-products which predominantly contain dienes and alkynes. Therefore, selective partial acetylene hydrogenation is crucial to increase the ethylene concentration by consuming the acetylene and avoiding further hydrogenation to ethane. This is commonly conducted through the use of supported palladium-based catalysts [4, 13-15]. However, they require special modifications to minimize the complete hydrogenation to ethane.

In 1991, a study was reported on the application of single-site titanium atoms for epoxidation of alkenes and cyclohexene, where titanocene was grafted on porous silica [16]. Another study of Pd_n clusters ($1 \leq n \leq 30$) on magnesia surfaces proved that one palladium atom is sufficient for production of benzene [17]. Since then, subsequent preliminary model studies have established that there are numerous advantages of these single-site heterogeneous catalysts. Single-atom catalysts achieve maximum dispersion of the metal and offer new catalytic properties in addition to this atom efficiency. Mechanistic and kinetic studies, using both computational and experimental methods, show that new intermediates (especially short-lived transition states) become energetically accessible [18]. In some cases, single site heterogeneous catalysts show very high selectivity for well-defined molecular products, for example, these catalysts are used for the challenging nitroarene hydrogenation and found to have both high activity and selectivity [19]. Therefore, these single-atom catalysts (SACs) relate to catalytic schemes with atomic metal species on the support surface and are emerging as a new area in the catalysis community.

There has been considerable progress in developing synthesis methods and techniques for these single-atom catalysts. The focus of these developments has been centered on achieving high stability, particularly to avoid metal aggregation and to achieve more facile loading of catalysts.

However, optimizing the synthesis of these SACs has been a daunting task for the catalysis community because of the tendency for agglomeration of metal atoms either during the synthesis processes or the subsequent treatments [20]. Over the course of the last two decades, several approaches have been designed to isolate metal sites on catalyst supports which include (i) using very low metal loading [15, 21]; (ii) enhancing the metal–support interactions [22, 23];

and (iii) utilizing vacancy defects on supports [24-26]. These strategies are aimed at preventing aggregation of the metal atoms by strengthening the metal–support interactions. For instance, zeolites are known to have a porous architecture with local binding sites to stabilize metal atoms against aggregation during the catalytic process [27, 28]. Also, defects on reducible oxides (*e.g.*, CeO₂ and TiO₂) aid in stabilizing singly distributed metal centers on support [29, 30].

Our group has conducted experiments to develop a metal-ligand self-assembly strategy [31-33] that adds metal-ligand interactions as a stabilizing effect for metal SACs on high surface area oxide powder supports [34-38]. These ligand-coordinated supported catalysts (LCSCs) allow high metal loading and also offer an opportunity to tune the chemical behavior of the metal center, while maintaining intimate contact between the metal and support. In this study, we examine the activity and selectivity of single-site Pd catalysts functionalized with 1,10-phenanthroline-5,6-dione (PDO) ligands (Figure 1) on high surface area CeO₂ powders for the hydrogenation of acetylene. PDO, a diketone-functionalized phenanthroline, was chosen as the ligand because its oxidative potential is suitable for stabilizing metal cations in a well-defined oxidation state. The amount of ligand introduced during the catalyst synthesis was varied and led to a surprisingly large effect on the selectivity of the hydrogenation reaction. By combining a set of experimental characterization tools, reaction studies, and DFT calculations, this work provides insight into the role of the PDO ligands in stabilizing the metal and in steering the reaction in the dynamic metal-ligand coordination environment on the oxide supports.

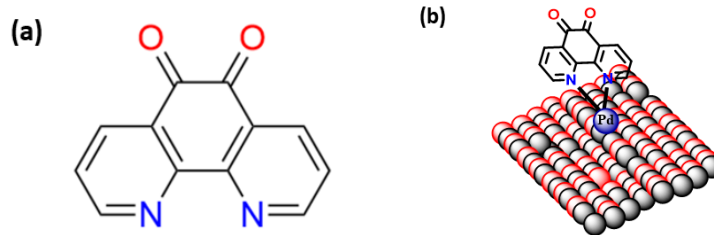


Figure 1. (a) Molecular structure of 1,10-phenanthroline-5,6-dione (PDO). (b) Schematic illustration of the LCSC design concept.

Methods

1. Single Atom Catalyst Synthesis

A modified wet impregnation synthesis method was used to prepare Pd-PDO catalysts on high surface area powder CeO₂ supports, as has been discussed in prior reports of other catalysts from our lab [39, 40]. Ten different mole ratios of PDO: Pd from 1:1 to 10:1 were used in the impregnation solution to vary the relative loading of Pd and PDO on the CeO₂ support.

Quantities of PDO (97% purity, Sigma Aldrich, Figure 1) in the range 2.94 – 29.4 mg (Table S1) were completely dissolved in 20 mL of distilled water by stirring for 20 min at room

temperature. 0.3 g CeO₂ (Alfa Aesar, 12.5 μm particle size) was added to the yellow PDO

solution. The mixture was then stirred for 1 h at room temperature. The Pd salt solution, 4.2 mg sodium tetrachloropalladate (97% purity, Sigma Aldrich) dissolved in 10 mL distilled water, was then added dropwise to the CeO₂/PDO/distilled water mixture under stirring over 30 minutes.

The Pd quantity was chosen to achieve a theoretical yield of 0.5 wt% Pd in the catalyst, although the actual loading is lower. The mixture was covered and stirred overnight, and then dried at room temperature under a flow of air. The dried catalyst was washed with water and then

dichloromethane (DCM) until powders did not show any yellow color (all free PDO was removed). XPS and ICP-MS were used to verify loading of the catalyst on the support. XRD, TEM and XAS analysis provided structural characterization.

2. Synthesis of Pd Nanoparticles on CeO₂

Pd nanoparticles were synthesized on the cerium oxide as a control sample for comparison to the single atom catalysts. The nanoparticles were loaded onto the CeO₂ powder using a traditional wet impregnation method [41]. 0.3 g of CeO₂ powder was dispersed in 20 mL of distilled water for 20 minutes. 4.2 mg of Na₂PdCl₄ was dissolved in 10 mL of distilled water and added dropwise into the CeO₂ solution. The mixture was stirred overnight and dried in an oven at 60 °C. The dried catalyst was heated at 300 °C for 6 hours in a reductive gas flow (H₂ and Ar) to produce reduced Pd nanoparticles on CeO₂. An additional reducing pre-treatment under H₂ flow for 1 h at 100 °C was tested but found to not improve the catalytic performance (see Section S3 of the Supporting Information). Therefore, the Pd nanoparticle catalysts discussed herein are used without pre-treatment. Note that the reductive treatment at elevated temperature was only applied to the Pd nanoparticle catalysts to follow common practices for nanoparticle catalyst synthesis, but this treatment was not done on the Pd-PDO metal-ligand catalysts.

3. Catalyst characterization

X-ray diffraction (XRD) was used to check for significant Pd nanoparticle aggregates, which were not detected on the single site catalysts. Transmission electron microscopy (TEM)

measurements were conducted on JEOL JEM 1400plus, which was operated at 120 kV to analyze catalyst structure and detect metal particle size. Catalysts were characterized by Inductively Coupled Plasma-Mass Spectroscopy (ICP-MS) to measure Pd loading on the catalyst. These measurements were performed with an Agilent 7700 quadrupole ICP-MS instrument. The catalysts were treated with aqua regia to completely dissolve Pd before measurement.

X-ray photoemission spectroscopy (XPS) measurements were performed with a PHI Versaprobe II XP spectrometer using a monochromated Al X-ray source. Small amounts of each of the catalyst powders were loaded and fixed onto a platen with double-sided tape. XPS spectra were collected for the following regions for each of the catalysts: Pd $3d$, N $1s$, C $1s$, Cl $2p$, Ce $3d$, and O $1s$. The binding energy (BE) was calibrated using the Ce $3d_{5/2}$ peak (882.0 eV). PDO/Pd and Cl/Pd mole ratios were quantified using the area ratio between the N $1s$ peak or Cl $3p$ peak and Pd $3d$ peak (Table 1). XPS peak fitting was performed using CasaXPS software.

X-ray absorption spectroscopy (XAS) measurements of the Pd K edge (24.4 keV) were performed at the 20-BM beamline at the Advanced Photon Source of Argonne National Laboratory. The monochromatized X-ray energy was calibrated with the Pd K-edge (24.4 eV). XAS of Pd foil, PdO₂ pellet, and (NH₄)₂PdCl₄ pellet were measured as standard references for Pd(0) and Pd(+2) in different coordination environments. Extended X-Ray Absorption Fine Structure (EXAFS) was analyzed to determine the coordination environment of the Pd centers. Since the Pd-O and Pd-N bond lengths are so similar, these are fit as a single “Pd-O/N” shell.

CO adsorption experiments were performed using a diffuse reflectance IR environmental chamber (PIKE Technologies, 162-4160, HTV) at room temperature (24 °C). Background spectra were collected under Ar flow before purging the chamber with 10% CO in Ar. After

flowing CO into the chamber for 15 min, the chamber was purged with pure Ar for 15 min to remove gas phase CO, as well as weakly adsorbed CO from the catalyst surface. Diffuse Reflectance Infrared Fourier Transform Spectra (DRIFTS) were collected with a IS20 FTIR spectrometer (Nicolet). Each DRIFTS spectrum was an average of 500 scans and was converted into Kubelka–Munk units.

4. Catalytic reaction studies

In this study, a catalytic flow reactor was used to study the activity and selectivity of the different catalysts synthesized. In each experiment, 50 mg of a catalyst was packed in a quartz tube and held in place at both ends with fiber glass wool. A reaction mixture consisting of hydrogen (8 sccm), acetylene (0.4 sccm), and argon (31.6 sccm) was flowed through the tube while the temperature of the catalyst was increased from 30 °C to 120 °C, where it was held during the course of the reaction. Acetylene conversion was monitored by mass spectrometer and used to quantify the activity of the catalyst.

5. DFT Calculations

We performed density functional theory (DFT) simulations using the Vienna Ab-initio Simulation Package (VASP) [42, 43] employing the projector-augmented wave (PAW) [44, 45] and plane wave basis set methods. We used the generalized gradient approximation (GGA) proposed by Perdew, Burke, and Ernzerhof (PBE) [46] to describe the exchange-correlation of electrons and the DFT-D3 method [47] to account for van der Waals interactions. We set the energy cutoff for planewave expansion at 500 eV. We use DFT+U approach [48] to introduce a

Hubbard-like term to account for the on-site interactions of localized Ce 4f electrons. The U-parameter is set to 5 eV [49]. We model the CeO₂ surface with a three-layer CeO₂(111). For the Pd-PDO complex adsorbed on the CeO₂(111) surface with the ratio of 1:1 or 1:2, our supercell consists of one Pd atom and one or two PDO ligands, respectively. All together, we thus have either 229 or 266 atoms in the Pd-PDO/CeO₂(111) supercell. Given the large number of atoms in the supercell, we sampled the Brillouin Zone only at the Γ point, for computational feasibility. During relaxation, the bottom layer of CeO₂(111) is held fixed. A vacuum slab of 15 Å was used in the direction normal to the plane of CeO₂(111) to ensure the absence of interlayer interactions in that direction. All structures are relaxed until all force components acting on each ion reach a threshold of 0.02 eV/Å.

Results and Discussion

1. Loading and complexation of Pd-PDO on support surface

Pd-PDO catalysts were synthesized with a range of PDO:Pd precursor mole ratios using our wet-impregnation method in order to determine the effect of this ratio on the loading, which was measured by both XPS and ICP-MS (Table 1). The PDO/Pd ratio on the catalyst surface measured by XPS increases with, but is significantly less than, the precursor solution ratio. The lower loading ratio indicates that a substantial amount of the ligand is washed away in the DCM and distilled water rinsing steps. With increasing precursor solution ligand ratio, it was observed that the Cl/Pd XPS area ratio decreased, indicating that the residual Cl from the Pd precursor is displaced by PDO coordination when excess PDO is available.

The metal loading measured by ICP-MS is about 0.11 wt. % (relative to CeO₂) for each of the catalysts, which is lower than the 0.50 wt. % of Pd in the precursor solution. A significant fraction of the Pd likely forms complexes with PDO in solution in such a way that prevents binding and loading of the metal to the support and is subsequently rinsed from the catalyst powder.

Table 1. Pd-PDO LCSCs were characterized by ICP-MS to determine Pd loading (column 2) and by XPS to determine PDO/Pd mole ratio and Cl/Pd mole ratio, before and after reaction. As the ratio of PDO to Pd precursor in the catalyst synthesis solution increases (column 1), there is an increase in the loading of PDO on the catalyst (column 3) and a decrease in the Cl content on the catalyst (column 4). On average for the Pd-PDO LCSCs, the PDO:Pd ratio decreases by 27 % after reaction (column 5) and the Cl:Pd ratio decreases by 38 % (column 6).

Synthesis PDO:Pd precursor ratio	Pre-reaction ICP-MS	Pre-reaction XPS		Post-reaction XPS	
	Pd Loading (wt.%)	PDO:Pd ratio	Cl:Pd ratio	PDO:Pd ratio	Cl:Pd ratio
1	0.13	0.64	0.83	0.61	0.51
2	0.11	1.26	0.59	0.84	0.27
3	0.12	1.53	0.76	1.01	0.27
4	0.10	1.34	0.88	1.22	0.66
5	0.09	2.34	0.43	1.56	0.39
6	0.10	3.12	0.35	1.70	0.23
0 (no PDO)	0.49	---	0.66	---	0.30

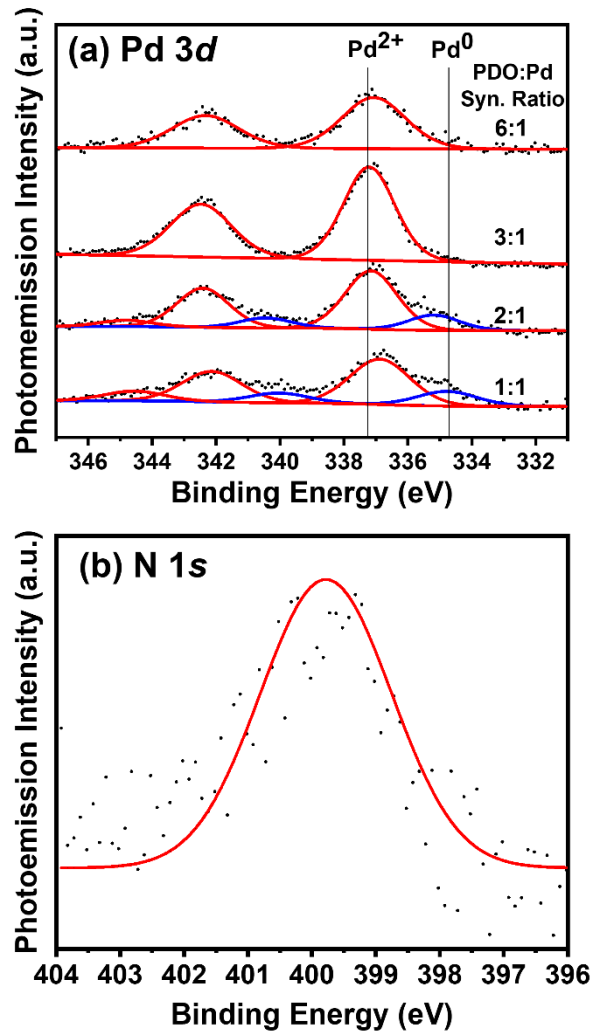


Figure 2. (a) Pd 3d XP Spectra of LCSCs with increasing PDO:Pd synthesis ratios. The peak at 337.3 eV is ascribed to Pd²⁺ and the peak at 335 eV is ascribed to metallic Pd on the support. (b) N 1s XPS of 1:1 PDO:Pd LCSC, indicating adsorption of PDO on the catalyst.

XPS measurement of Pd 3d (Figure 2) for PDO:Pd ratios shows a predominant peak at a binding energy of 337.3 eV, consistent with a Pd oxidation state of +2 [50]. At PDO:Pd synthesis ratios of 2:1 and 1:1, there is also some intensity at 335 eV, which corresponds to metallic Pd⁰ [51]. These data indicate that the majority of the Pd loaded on the support in the presence of

PDO is coordinated to one or two PDO ligands to maintain the Pd²⁺ oxidation state. The N 1s signal from PDO is recorded at 399.8 eV (Figure 2b).

X-ray diffraction measurements, which should detect crystalline metal nanoparticles larger than ~2-3 nm in size, did not detect any Pd aggregation for the 1:1 catalyst (Figure S4). Transmission electron microscopy was used to image both fresh and used catalysts. There were no nanoparticles detected for the fresh single site Pd-PDO catalysts (Figure 3a). Even for the Pd-PDO catalysts that had undergone reaction conditions and temperatures up to 120 °C for 14 hours, there were no nanoparticles detected in TEM images (Figure 3b). In TEM measurements of reduced Pd nanoparticles on CeO₂ (no PDO present), nanoparticles 2 nm in size were observed (Figure 3c). The loading of the Pd precursor in the synthesis solution was 0.5 wt % for both the single site catalysts and the control study of nanoparticles on CeO₂, however, the actual loading measured by ICP-MS is only around 0.1 wt% for the Pd-PDO, but 0.5 wt% for Pd nanoparticles, thus there is much more metal available for aggregation in the latter sample. The difference in actual loading is likely due to ligand stabilization of the metal in the solution state during the loading process, which would be rinsed away in a later step of the catalyst synthesis.

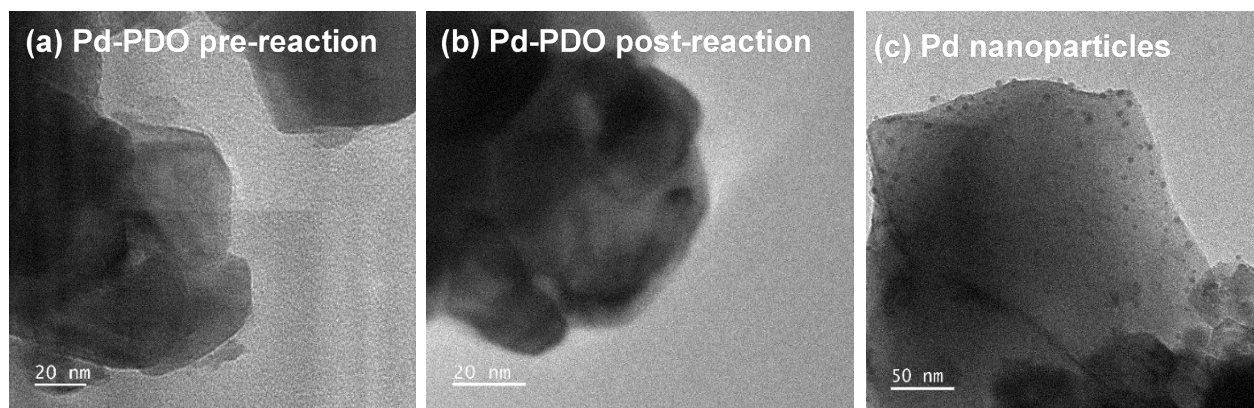


Figure 3. TEM images of Pd-PDO LCSC with PDO:Pd precursor ratio of 1:1 (a) before and (b) after reaction. No nanoparticles were observed for the LCSC. (c) TEM image of Pd nanoparticles on CeO₂. The nanoparticles were formed by heating the Pd/CeO₂ without ligand for 6 hours at 450 °C.

CO adsorption experiments were conducted to probe the active sites on the catalyst surface. Experiments were conducted under a gas mixture of 10% CO and 90% Ar at room temperature. As shown in Figure 4, DRIFTS spectra recorded on CeO₂ samples with and without Pd loading show two characteristic peaks of CO gas at 2175 cm⁻¹ and 2120 cm⁻¹ [52]. For the CeO₂ with Pd-PDO loading, there are additional features at 2100 cm⁻¹ and 1950 cm⁻¹ (Figure 4, subtracted spectrum). The peak at 2100 cm⁻¹ is due to CO being linearly adsorbed on top of single sites present on our catalyst surface [21]. The small peak at 1950 cm⁻¹ is due to CO being adsorbed in a bridged mode on top of two neighboring Pd atoms on the catalyst surface [21, 53, 54]. The relative sizes of these features indicates that the majority of the adsorbed CO adopts the linear adsorption configuration on single atom Pd.

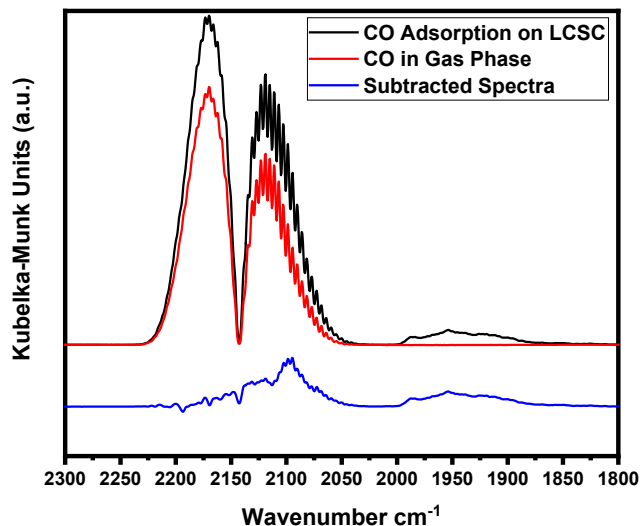


Figure 4. DRIFTS Spectra using CO as a probe to determine the nature of active sites on the catalyst surface. The spectrum labelled “gas phase” (red) is measured on CeO₂ powder with no catalyst loading and thus shows only gas phase CO. This is subtracted from the Pd-PDO/CeO₂ LCSC peak (black) to demonstrate the CO adsorbing on the surface (blue).

2. Pd Coordination Environment Analysis

Catalysts with varying synthesis ratios of PDO: Pd were examined by EXAFS for the presence, if any, of the Pd-Pd bond as well as exploring the changes in the Pd coordination environment that could be contributing to changes in activity and selectivity of the catalysts. Experiments were conducted with six ligand: Pd synthesis ratios from 1:1 to 6:1. The Pd-Pd bond at 2.4 Å was not observed for any of these catalysts (e.g., Figure 5b for 1:1), indicating significant Pd aggregation is not present in these systems. In the absence of PDO ligand, the Pd-Pd bond at 2.4 Å was present for the reduced Pd/CeO₂ catalyst indicating the formation of Pd nanoparticles (Figure 5a).

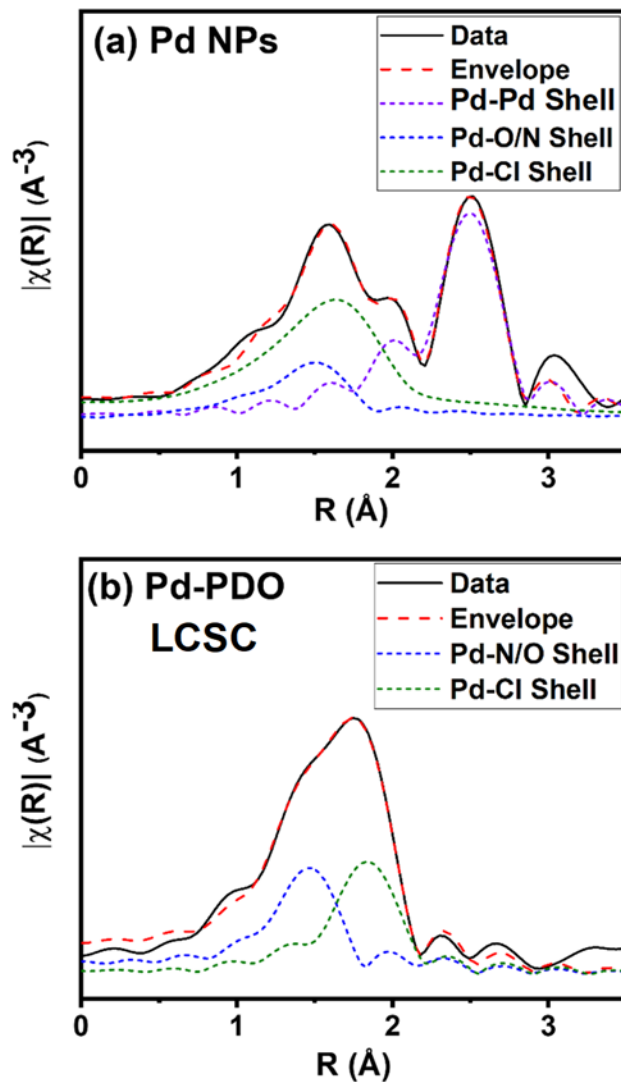


Figure 5. EXAFS spectra and fitting for (a) Pd nanoparticles on CeO_2 and (b) Pd LCSC with PDO:Pd precursor ratio of 1:1. No peaks for Pd-Pd were observed for the LCSC.

With increasing synthesis ratios of PDO:Pd, the coordination number of Pd-Cl decreased (Table 2). This trend further confirms the XPS result that shows a decrease in the amount of chloride present in samples with high synthesis ligand ratios (Table 1). Together, these results

point to the possibility that the chloride from the metal precursor is displaced from the catalyst by the availability of excess ligand as more ligand is added during synthesis.

We measured a lower Pd-O/N coordination number for 1:1 PDO:Pd compared to higher synthesis ligand ratios of PDO:Pd (Table 2). Although this change was subtle, it pointed to the possibility of Pd sites interacting with more than one ligand molecule at a given active site.

Table 2. EXAFS fitting for varying PDO:Pd precursor ratios. The overall fit had two components consisting of a Pd-O/N shell and a Pd-Cl shell. *N* in the Table represents the coordination numbers of Pd with Cl and O/N. *R* represents the bond lengths for each of these fitting shells. The *k* range used for Fourier transformation of each measurement was 0–15Å⁻¹.

PDO:Pd Ratio	Pd-Cl	Pd-O/N
	<i>N</i>	<i>N</i>
1:1	1.9 (± 0.2)	1.7 (± 0.3)
2:1	1.3 (± 0.3)	2.7 (± 0.4)
3:1	1.7 (± 0.3)	2.2 (± 0.5)
4:1	1.9 (± 0.3)	1.9 (± 0.4)
5:1	1.8 (± 0.3)	2.1 (± 0.5)
6:1	1.3 (± 0.5)	2.0 (± 0.6)

Since EXAFS is not able to distinguish between binding Pd on the O vs. N binding sites on PDO, we applied Density Functional Theory (DFT) calculations to investigate the binding of the Pd at these binding pockets. We found that the binding of the Pd through the nitrogen pocket of the ligand has a lower formation energy (– 1.82 eV) compared to the oxygen pocket (– 1.37 eV, (Table S3). We also investigated the binding of the Pd atom to two PDO ligand molecules

through both N pockets, both O pockets, or one of each type of pocket and found the latter to be the most stable (Table S4).

Since ceria, a reducible oxide, is used as a support for the catalysts, we further investigated the formation of vacancies on the ceria support. Reducible oxides are strongly influenced by the reversible oxidation state of the metal. Due to this reversibility, these materials are able to store and release oxygen for different catalytic processes. For ceria, a reduction in the oxidation number of the cerium occurs when the crystal loses an oxygen atom to form a vacancy. The crystal is also able to form a cerium vacancy at higher temperatures by losing a cerium atom from the (111) surface of the oxide. Atomistic models of the two vacancies are shown in Figures 6a and 6b. The formation energy of an oxygen vacancy on ceria is much smaller than for a cerium vacancy (4.410 eV and 11.321 eV, respectively), so oxygen vacancies are more likely to form. Furthermore, Pd bound to the oxygen vacancy has a formation energy that is lower than that of the vacancy alone (Table S5, also lower than Pd binding at Ce vacancies), indicating a favorable adsorption energy for Pd at the O vacancy of -3.152 eV.

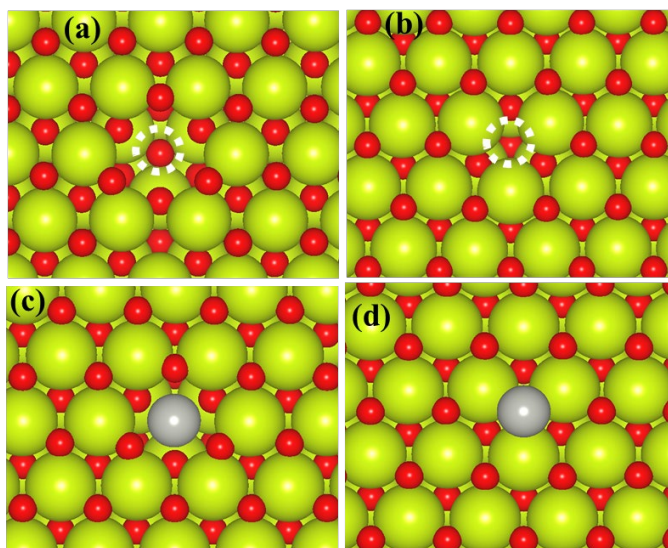


Figure 6. Schematic representation of CeO₂ (111) surface with single (a) Ce or (b) O vacancy (indicated by white dashed circle). Pd adsorption at (c) Ce or (d) O vacancy site. Green, red, and grey balls represent Ce, O, and Pd atoms, respectively.

PDO ligand binding to Pd is an essential part of our catalyst composition. Electron density difference plots comparing Pd/CeO₂ bound to one or two PDO molecules (Figure 7) show further oxidation of Pd upon introducing the second PDO ligand. The electron density difference contours around Pd suggest that there is electron depletion at the Pd site in the presence of one PDO ligand but the magnitude of electron depletion is greater for Pd with two PDO ligands.

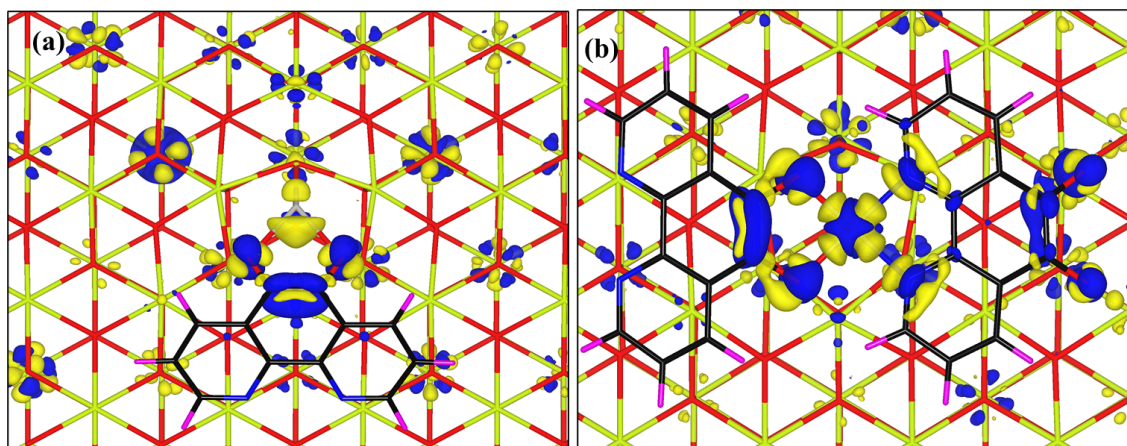


Figure 7. Plots of the electron density difference calculated for (a) Pd-PDO/CeO₂(111) and (b) Pd-(PDO)₂/CeO₂(111). The electron accumulation (blue) and electron depletion (yellow) isosurfaces are plotted with contour values of 0.01 and $-0.01 \text{ e}/\text{\AA}^3$, respectively.

3. Experimental measurements of activity and selectivity

Each of the catalysts (over a range of synthesis ligand ratios) were tested for activity and selectivity using a flow reactor. Activity was calculated from the conversion of acetylene and selectivity was calculated based on the production of ethylene relative to the acetylene consumed. The summarized results for activity and selectivity of ethylene for each of these catalysts are shown in Figures 8a and 8b, respectively. For comparison, the catalyst with Pd nanoparticles without any ligand was also tested and showed 100% conversion to ethane, *i.e.*, no selectivity for ethylene. The activity of the LCSCs decreased with increasing synthesis ligand ratios.

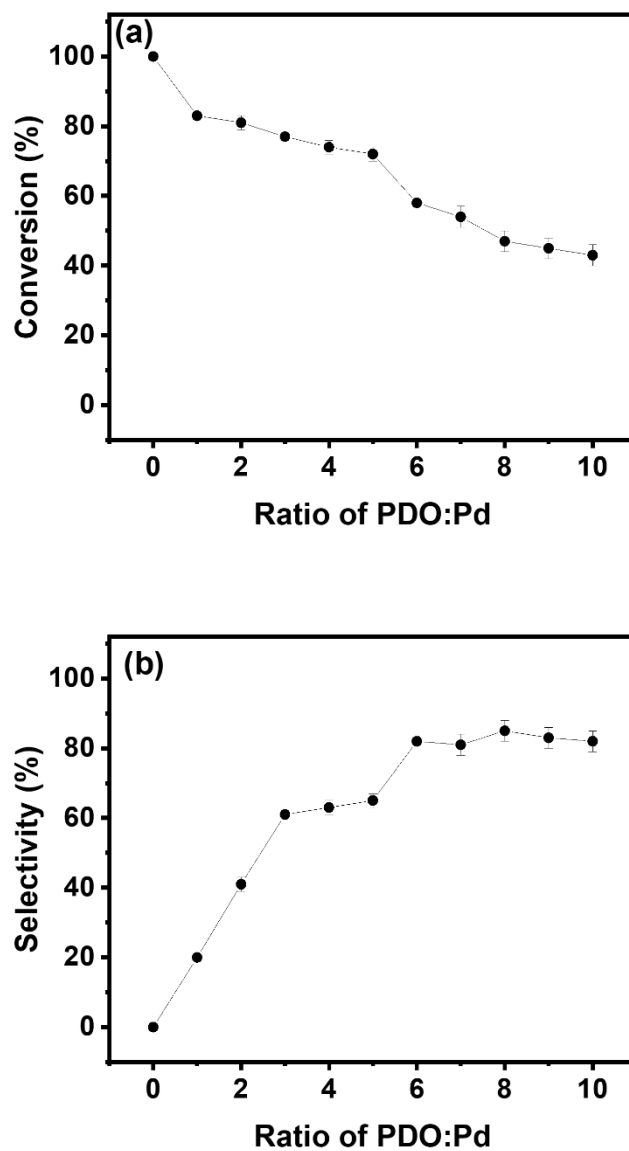


Figure 8. (a) Acetylene conversion (catalyst activity) and (b) selectivity for ethylene for a series of Pd-PDO LCSCs with increasing PDO:Pd precursor ratios from 0 to 10 (plotted on horizontal axis). Conversion and selectivity were measured at 120 °C.

Selectivity for ethylene increased with increasing synthesis ratio, with the lowest selectivity being 30 % for the PDO:Pd (1:1)/CeO₂ catalyst and highest selectivity recorded at 80 % for the PDO:Pd (6:1)/CeO₂ catalyst. The selectivity of the catalysts with ligand ratios greater than 6:1 (we tested up to 10:1) did not further increase beyond 80 %, indicating that the ligand molecules had completely saturated the Pd single sites. With increasing PDO:Pd ratio, there is a greater opportunity for Pd to complex with one or more PDO ligands.

4. Post Reaction Analysis and Stability of LCSCs

The Pd 3d spectra for the post reaction catalysts are unchanged relative to before the reaction (compare Figures 2a and S2). At the lowest PDO:Pd ratios, there was a slight increase in the peak area for metallic Pd, but each of the spectra still show the majority of the Pd in the 2+ oxidation state. The N 1s shows some loss of ligand after the reaction, which is more noticeable on the catalysts that started with a higher ligand ratio. Each of the ligand:metal ratios decreases to less than 2:1, which is more consistent with a two dimensional ligand-metal coordination structure at the surface compared to some of the higher ratios (up to 3) observed before the reaction as shown in Table 1. There was a significant reduction in the Cl content on the surface, indicating that residual Cl from the metal precursor is displaced from the active sites during the reaction.

The Pd-PDO catalysts showed excellent stability over many hours. For example, steady activity was observed over ~15 hours for 1:1, 4:1, and 6:1 PDO:Pd synthesis ratios (Figures S6, S7 and S8 respectively). Post-reaction XPS does shows a loss of ligand (27 % decrease in PDO:Pd ratio, Table 1) as compared to the fresh catalyst, which indicates that there may be some

LCSC decomposition in the early stage of reaction, but, in spite of this, the reaction maintains a steady performance for several hours. However, XPS measurements of Pd metal are virtually unchanged after reaction, indicating a stable Pd²⁺ oxidation state and isolation of the metal atoms (compare Figures 2 and S2).

5. Insight from DFT modeling of reaction intermediates about reaction selectivity

The adsorption energy (E_{ads}) of hydrogen, acetylene, and ethane on a single Pd atom at an oxygen vacancy of the ceria surface was calculated using DFT (Figure S9) with no PDO present. Although this is a single Pd atom (no ligand), we find the adsorption of ethylene on the Pd atom ($E_{ads} = -0.85$ eV) to be energetically more favorable than that of acetylene ($E_{ads} = -0.77$ eV), indicating that single Pd can potentially stabilize ethylene for hydrogenation just as well as it can acetylene. This result indicates that single atom character alone may not be sufficient to enable the high reaction selectivity observed experimentally for Pd-PDO, but there may be other effects due to the presence of PDO ligands.

We calculated the stability of several reaction intermediates that may exist during the course of hydrogenation of acetylene over the Pd-(PDO)₁ complex supported by ceria (Figure 9). Calculation of full reaction pathways was prohibitively expensive for these systems, but we interpret energy minimization calculations to develop new insight. To evaluate the selectivity for ethylene, we compare formation energy values for key states of the system that would steer the reaction toward ethylene vs. ethane products. In the case of Pd-(PDO)₁ on CeO₂(111), the addition of H to the C₂H₄* intermediate has an energy cost of 0.92 eV, but this is lower than the 1.36 eV energy difference for desorption of ethylene. This implies that the Pd-(PDO)₁ single-site

catalyst may tend toward complete hydrogenation to ethane. We also note that the location and coordination of the Pd atom change substantially with the adsorption of the different reaction intermediates. Upon desorption of the ethylene (Figure 9c), the Pd adatom moves closer to the CeO₂ surface ($\Delta h \sim 0.81 \text{ \AA}$), presumably to stabilize its local coordination environment, thereby allowing a reversible interaction between the metal-ligand complex and the support to facilitate hydrogenation catalysis.

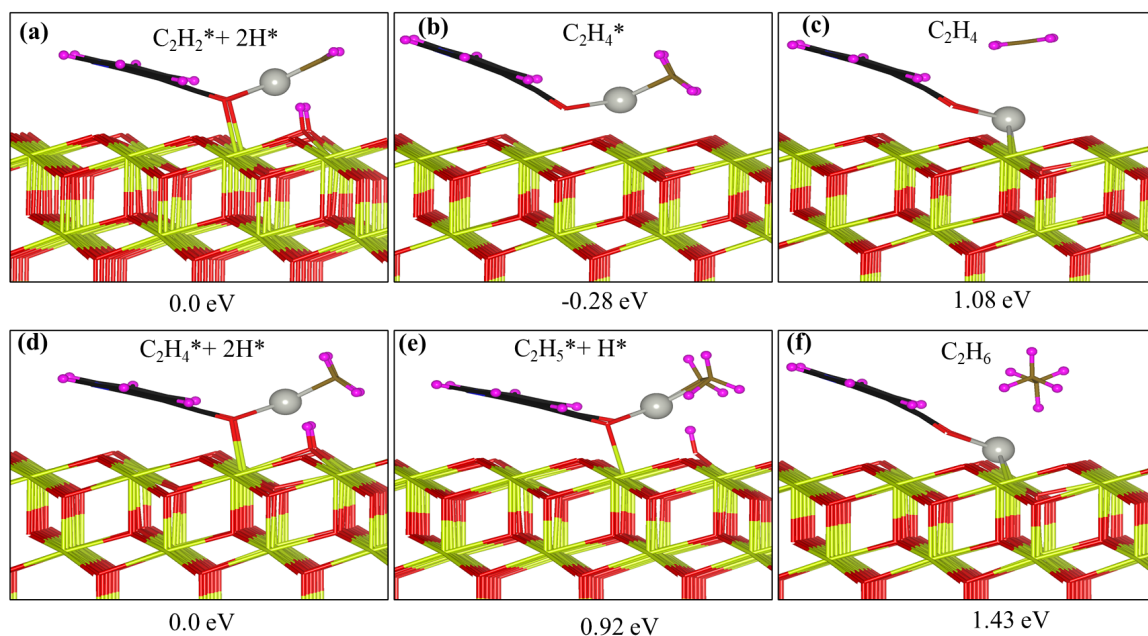


Figure 9. Snapshots from DFT energy minimization calculations for Pd-PDO (one of each) on CeO₂ at different stages of the acetylene hydrogenation reaction. Top row: (a) adsorption of acetylene at Pd and of 2 H at CeO₂, (b) adsorption of ethylene at Pd, and (c) desorption of ethylene. Bottom row: (d) ethylene adsorption at Pd and 2 H at CeO₂, (e) ethyl adsorption at Pd and H at CeO₂, and (f) ethane desorption. The formation energy values under each panel are relative to the left panel of each row.

Our experimental results indicate significant differences in reaction selectivity for ethylene at higher ligand ratios, so we also conducted DFT analysis of reaction intermediates on Pd bound to two PDO ligands, Pd-(PDO)₂. The ligand orientation allows Pd binding at the O pocket of one ligand and the N pocket of the other ligand, which was found to be the most favorable configuration (Table S4). We examined the stability of C₂H₄ (Figure 10) and C₂H₂ (Figure 11) adsorption on three different starting configurations involving Pd coordination with two PDO ligands with different initial bond lengths. In each case, either C₂H₂ or C₂H₄ is attached to Pd from the top side, but the PDO molecules are positioned so that either one ligand is attached to Pd (Figures 10a, 10b, 11a, and 11b) or both PDO are attached (Figures 10c and 11c). These are the starting configurations for the calculations that will allow us to see how the adsorption is affected as the system is allowed to relax.

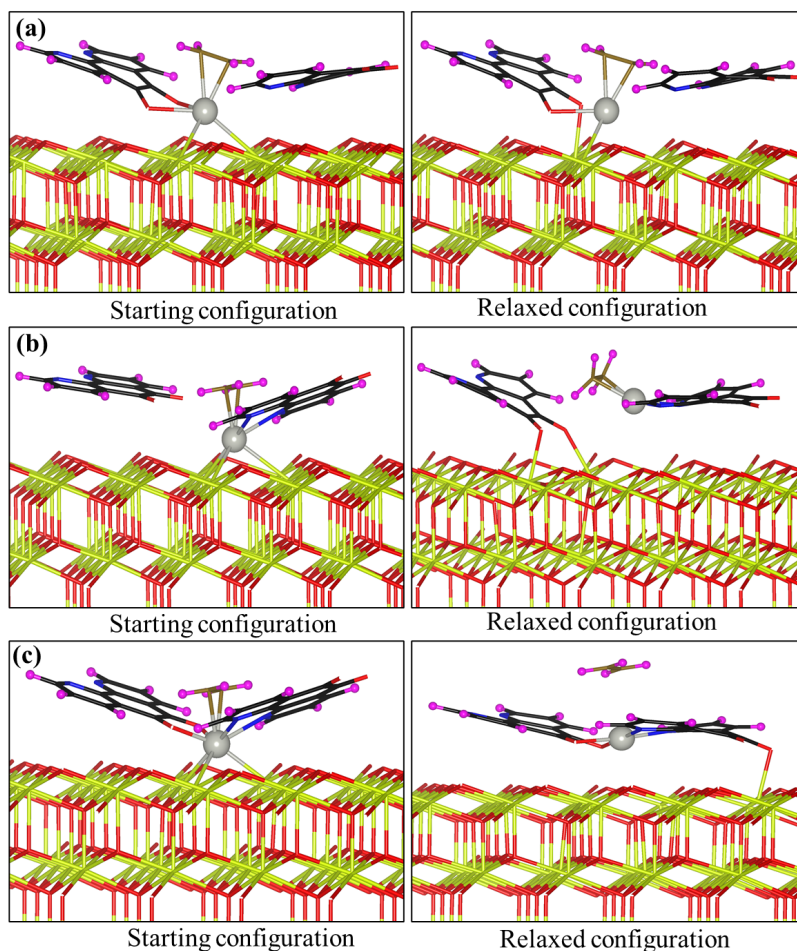


Figure 10. (a) Pd with two PDO ligands and ethylene on CeO₂. The starting configuration (left) was designed to have the second PDO in the vicinity of the Pd active site, but not directly bound to it. During relaxation Pd lose one of its bonds with O of the ketone, and one of Pd-Ce bonds, *i.e.*, PDO is stable in this loosely associated state. (b) Ethylene adsorption on Pd in the vicinity of two PDO molecules on CeO₂. The starting configuration (left) has ethylene bound to Pd, but one PDO molecule is relatively far away. In the relaxed configuration (right), PDO shows binding to CeO₂ through the ketone O atoms and the Pd to CeO₂ distance is larger. (c) Ethylene desorption on Pd in the vicinity of two PDO molecules on CeO₂. The starting configuration (left) has ethylene bound to Pd-(PDO)₂. In the relaxed configuration, the ethylene desorbs from the active site and the Pd-Ce bond is lengthened.

Pd coordinated to one PDO molecule on CeO₂ shows stable adsorption of C₂H₄ (Figure 10a). While the stability of C₂H₄ against desorption from this Pd site does not promote high selectivity for C₂H₄ as the end product, it tends to facilitate further hydrogenation to C₂H₆. As shown in Figure 10b the second PDO molecule can, however, bind itself to the CeO₂ support and this process is downhill in energy by – 1.20 eV relative to the ionically relaxed configuration shown in Figure 10a. On the other hand, when two PDO molecules are near the Pd active site, we find that the C₂H₄ adsorption is destabilized. To illustrate this, we proceed with a DFT calculation with an initial configuration of one PDO and one C₂H₄ bound to Pd with a second PDO nearby (Figure 10c), to find that the system relaxes to a configuration of quasi square planar coordination of two PDOs around the Pd atom and the ethylene molecule desorbed to the gas phase. This process is downhill in energy by – 2.14 eV relative to the relaxed configuration shown in Figure 10a. The Pd-Ce bond changes by 0.5 Å when the second PDO ligand binds to Pd (Figure 10c) compared to just one PDO attached (Figure 10b), indicating that the Pd-PDO active site can lift itself from the ceria support during the course of the reaction.

Figure 11a illustrates the spontaneous destabilization of the acetylene from the active site. The Pd-(PDO)₂ complex elongates the Pd-Ce bond again. Figure 11b shows that the binding of the second PDO molecule to the Pd-PDO-acetylene complex can lead to the elongation of the Pd-Ce bond as well as the formation of a PDO-Pd bond. This process is downhill in energy by – 0.10eV relative to the relaxed configuration shown in Figure 11a. Similarly shown in the Figure 11c above, in the case of an acetylene molecule bound to a Pd-PDO active site, the adsorption of a second PDO molecule in the vicinity causes the Pd-PDO bound to the acetylene to elongate its Pd-Ce bond. This process is downhill in energy by – 0.98eV relative to the relaxed configuration shown in Figure 11a. These results support the experimental observations of the

loss of activity for higher ratios of the PDO: Pd complex by indicating that the acetylene can adsorb and interact with the Pd-(PDO)₂ complex and subsequently desorb from the catalyst surface without undergoing any hydrogenation.

In addition to the destabilization of the C₂H₄ adsorption, the two PDO configuration also offers a mechanistic pathway to facilitate acetylene hydrogenation. DFT calculations of dihydrogen adsorption on Pd in the vicinity of two PDO ligands shows that the individual H atoms can react with the ketone O of the PDO to form OH units on the molecule. The PDO-H₂ species separates from the Pd center in energy minimization calculations, indicating that the H addition to PDO destabilizes the M-L coupling as shown in Figure S10.

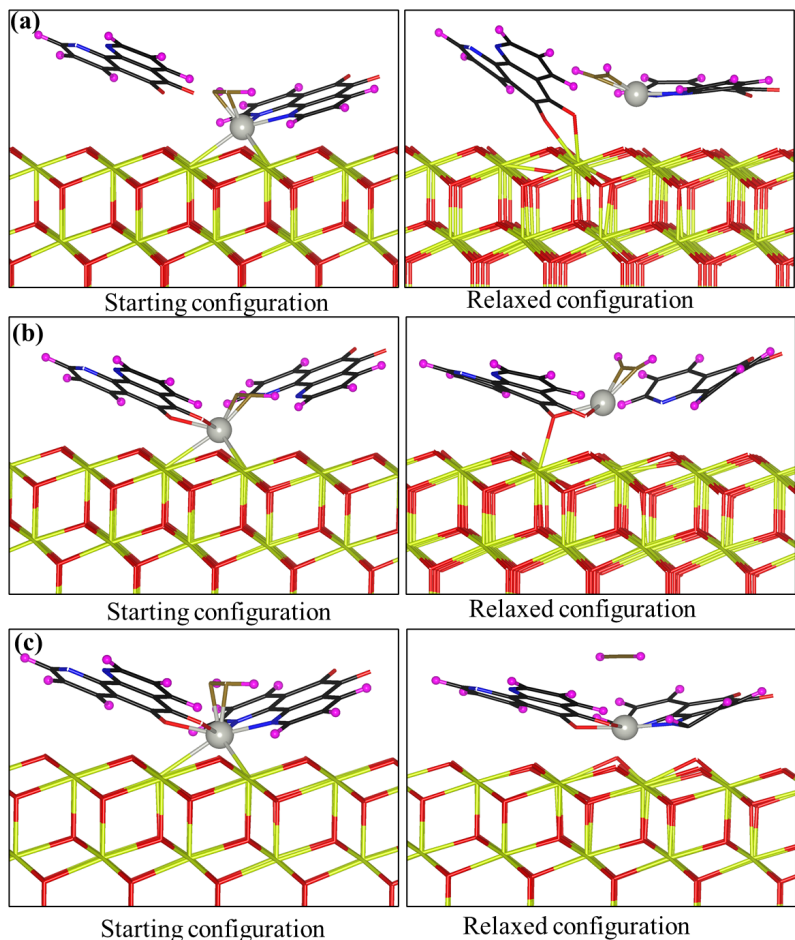


Figure 11. (a) Acetylene adsorption on Pd in the vicinity of two PDO molecules on CeO₂. The starting configuration (left) has acetylene bound to Pd-(PDO)₂ with one of the PDO molecules interacting directly with the CeO₂ support. In the relaxed configuration, the acetylene desorbs from the active site and the Pd-Ce bond is lengthened. The PDO molecule no longer interacts directly with the CeO₂ support. (b) Acetylene adsorption on Pd bound to two PDO molecules on CeO₂. The relaxed configuration (right) shows that the binding of acetylene leads to one of the Pd-Ce bonds to be elongated and a PDO-CeO₂ bond to form. (c) Starting configuration is designed so that the acetylene is somewhat distorted to allow for the second PDO to attach at Pd. Relaxed configuration shows the second PDO (left) binding to CeO₂ and the Pd at a larger distance from the CeO₂ surface.

We were interested in exploring whether this H addition to PDO could serve as a H source for acetylene hydrogenation. A calculation was set up with PDO-H₂ close to the Pd center and acetylene in an adsorbed state on the Pd and close to the PDO-H₂ as shown in Figure 12. These calculations demonstrated the ability of the ligand to deliver dissociated hydrogen to the Pd-PDO active site for the hydrogenation of acetylene to produce ethylene. This process was downhill in energy by – 3.14 eV. The ethylene formed during this process can desorb from the surface of the catalyst. Subsequent to the ethylene desorption in this calculation, the Pd binds to the second PDO molecule in the vicinity and becomes fully saturated as shown in Figure 12. The process is downhill in energy and therefore is favored. The reversible exchange of two H atoms on and off the PDO may contribute to the experimentally observed selectivity for partial hydrogenation of acetylene to ethylene as shown in Figure 12.

We note that the acetylene adsorption in the presence of PDO-H₂ leads to hydrogenation, but ethylene adsorption in the presence of PDO-H₂ does not lead to hydrogenation. Instead, the adsorbed ethylene spontaneously desorbs from the active site in the relaxed configuration as shown in Figure 13. This inhibition of hydrogenation of ethylene to ethane with 2 ligand molecules bound to the Pd can explain the experimental results that show an increase in selectivity to ethylene in higher ligand ratio catalysts.

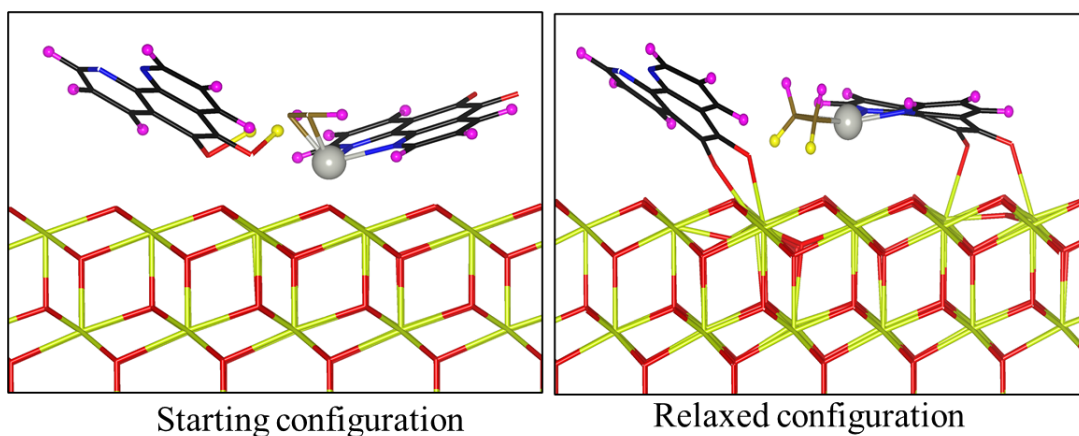


Figure 12. Starting configuration (left) of Pd-(PDO)₂ on CeO₂ with acetylene adsorbed on the Pd atom and two H atoms bound to the PDO molecule on the left at the diketone O atoms. The adsorbed acetylene is distorted away from sp geometry. After energy relaxation in DFT, the relaxed configuration (right) is obtained in which the two H atoms have bonded with acetylene to form ethylene.

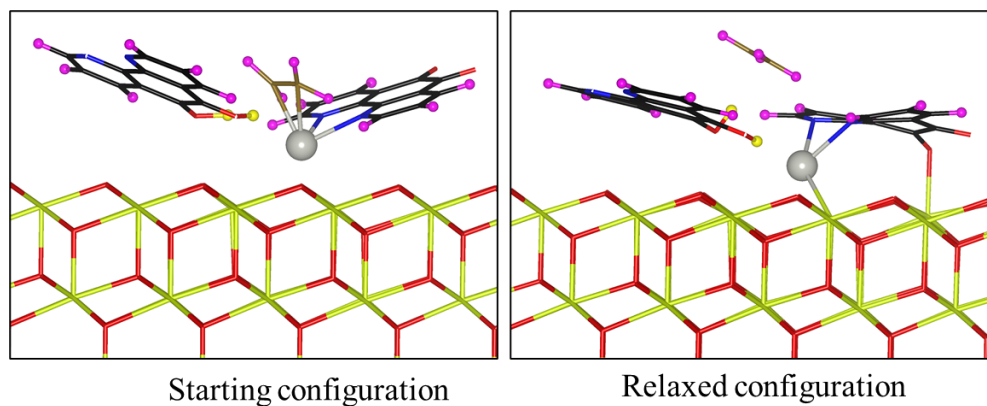


Figure 13. Starting configuration (left) of Pd-(PDO)₂ on CeO₂ with ethylene adsorbed on the Pd atom and two H atoms bound to the PDO molecule on the left at the diketone O atoms. The adsorbed ethylene is distorted away from sp² geometry. In the presence of PDO-H₂ ethylene does not undergo further hydrogenation. After energy relaxation in DFT, the relaxed configuration (right) is obtained in which the ethylene desorbs from the Pd atom.

Conclusions

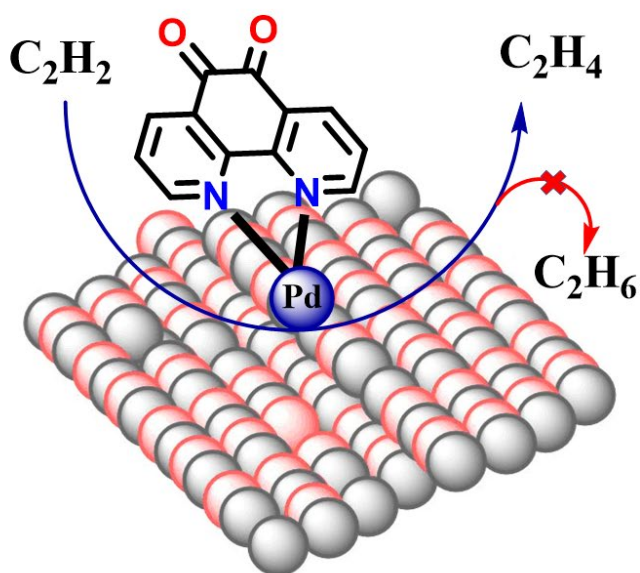
Ligand-coordinated CeO₂-supported Pd catalysts are active for acetylene hydrogenation under mild conditions with a strong dependence of selectivity for ethylene on ligand:metal ratio. Higher ratios show a significant improvement in the selectivity of the catalyst toward ethylene production rather than over-hydrogenation to ethane. These heterogeneous catalysts mostly contain atomically-dispersed Pd²⁺ sites. We demonstrated a clear trend of increasing selectivity with increasing ligand:metal ratio. DFT calculations of these LCSCs provide insight into the reaction mechanism, especially that the ability of the PDO ligand to shuttle hydrogen to the active site may be significant in promoting the selective behavior of the catalyst. These results show that on-surface metal-ligand coordination of single-atom catalyst centers can be an effective approach to tune catalyst activity and selectivity, especially in a dynamic metal-ligand coordination environment, for highly active single atom catalysts.

Acknowledgements

This work was supported by the U. S. Department of Energy, Office of Basic Energy Sciences, Chemical Sciences program, DE-SC0021390 (SLT) and by the National Science Foundation, NSF CHE1955343 (TSR). XPS measurements were carried out at the Indiana University (IU) Nanoscale Characterization Facility, with assistance from Dr. Yaroslav Lasovyy. XAS measurements were performed at beamline 9-BM at the Advanced Photon Source, an Office of Science User Facility operated for the U.S. Department of Energy (DOE) Office of Science by Argonne National Laboratory, under Contract No. DE-AC02-06CH11357. ICP-MS measurements were performed in IU Department of Earth and Atmospheric Sciences by Dr.

Shelby Rader. Transmission electron microscopy (TEM) measurements were performed at the IU Electron Microscopy Center by Dr. Xun Zhan. Computational resources were provided by the National Energy Research Scientific Computing Center (NERSC) and the UCF's Advanced Research Computing Center (ARCC).

Table of Contents Graphic



References

- [1] A. Ibhaddon, S. Kansal, The Reduction of Alkynes Over Pd-Based Catalyst Materials - A Pathway to Chemical Synthesis, *Journal of Chemical Engineering & Process Technology*, 09 (2⁰17).
- [2] D.V. Glyzdova, N.S. Smirnova, N.N. Leont'eva, E.Y. Gerasimov, I.P. Prosvirin, V.I. Vershinin, D.A. Shlyapin, P.G. Tsyru'nikov, Synthesis and Characterization of Sibunit-Supported Pd–Ga, Pd–Zn, and Pd–Ag Catalysts for Liquid-Phase Acetylene Hydrogenation, *Kinetics and Catalysis*, 58 (2017) 140-146.
- [3] S.F. Yuk, G. Collinge, M.-T. Nguyen, M.-S. Lee, V.-A. Glezakou, R. Rousseau, Selective Acetylene Hydrogenation over Single Metal Atoms Supported on Fe₃O₄(001): A first-Principle Study, 152 (2020) 154703.
- [4] Y. Cao, Z. Sui, Y. Zhu, X. Zhou, D. Chen, Selective Hydrogenation of Acetylene over Pd-In/Al₂O₃ Catalyst: Promotional Effect of Indium and Composition-Dependent Performance, *ACS Catal.*, 7 (2017) 7835-7846.
- [5] G. Watson, R. Wells, D. Willock, G. Hutchings, A Comparison of the Adsorption and Diffusion of Hydrogen on the {111} Surfaces of Ni, Pd, and Pt from Density Functional Theory Calculations, *Journal of Physical Chemistry B - J PHYS CHEM B*, 105 (2001).
- [6] B. Yang, R. Burch, C. Hardacre, G. Headdock, P. Hu, Origin of the Increase of Activity and Selectivity of Nickel Doped by Au, Ag, and Cu for Acetylene Hydrogenation, *ACS Catalysis*, 2 (2012) 1027-1032.
- [7] S.A. Nikolaev, V.V. Smirnov, A.Y. Vasil'kov, V.L. Podshibikhin, Synergism of the Catalytic Effect of Nanosized Gold-Nickel Catalysts in the Reaction of Selective Acetylene Hydrogenation to Ethylene, *Kinetics and Catalysis*, 51 (2010) 375-379.
- [8] F.-M. McKenna, R. Wells, J. Anderson, Enhanced Selectivity in Acetylene Hydrogenation by Ligand Modified Pd/TiO₂ catalysts, *Chemical communications (Cambridge, England)*, 47 (2011) 2351-2353.
- [9] G. Vilé, D. Albani, M. Nachtegaal, Z. Chen, D. Dontsova, M. Antonietti, N. López, J. Pérez-Ramírez, A Stable Single-Site Palladium Catalyst for Hydrogenations, *Angewandte Chemie International Edition*, 54 (2015) 11265-11269.
- [10] K.M. Sundaram, M.M. Shreehan, E.F. Olszewski, Ethylene, in: *Kirk-Othmer Encyclopedia of Chemical Technology*.
- [11] H.-F. Joaquin, L. Juan, Quantification of Poisons for Ziegler Natta Catalysts and Effects on the Production of Polypropylene by Gas Chromatographic with Simultaneous Detection: Pulsed Discharge Helium Ionization, Mass spectrometry and Flame Ionization, *J Chromatogr A*, 1614 (2020) 460736.
- [12] D. Duca, F. Frusteri, A. Parmaliana, G. Deganello, Selective Hydrogenation of Acetylene in Ethylene Feedstocks on Pd catalysts, *Applied Catalysis A: General*, 146 (1996) 269-284.
- [13] J.H. Kang, E.W. Shin, W.J. Kim, J.D. Park, S.H. Moon, Selective Hydrogenation of Acetylene on TiO₂-Added Pd Catalysts, *Journal of Catalysis*, 208 (2002) 310-320.
- [14] W.-J. Kim, S.H. Moon, Modified Pd catalysts for the Selective Hydrogenation of Acetylene, *Catalysis Today*, 185 (2012) 2-16.
- [15] A. Sárkány, A. Horváth, A. Beck, Hydrogenation of Acetylene over Low Loaded Pd and Pd-Au/SiO₂ Catalysts, *Applied Catalysis A: General*, 229 (2002) 117-125.
- [16] M.S. Wong, H.C. Huang, J.Y. Ying, Supramolecular-Templated Synthesis of Nanoporous Zirconia–Silica Catalysts, *Chemistry of Materials*, 14 (2002) 1961-1973.
- [17] S. Abbet, A. Sanchez, U. Heiz, W.D. Schneider, A.M. Ferrari, G. Pacchioni, N. Rösch, Acetylene Cyclotrimerization on Supported Size-Selected Pd_n Clusters (1 ≤ n ≤ 30): One Atom Is Enough!, *Journal of the American Chemical Society*, 122 (2000) 3453-3457.
- [18] J.M. Thomas, R. Raja, D.W. Lewis, Single-Site Heterogeneous Catalysts, *Angewandte Chemie International Edition*, 44 (2005) 6456-6482.

- [19] L. Wang, E. Guan, J. Zhang, J. Yang, Y. Zhu, Y. Han, M. Yang, C. Cen, G. Fu, B.C. Gates, F.-S. Xiao, Single-Site Catalyst Promoters Accelerate Metal-Catalyzed Nitroarene Hydrogenation, *Nature Communications*, 9 (2018) 1362.
- [20] S. Ji, Y. Chen, X. Wang, Z. Zhang, D. Wang, Y. Li, Chemical Synthesis of Single Atomic Site Catalysts, *Chemical Reviews*, (2020).
- [21] F. Yang, J. Tang, B. Shao, S. Gao, X. Liu, Ni-Bearing Nanoporous Alumina Loaded Ultralow-Concentrated Pd as Robust Dual Catalyst Toward Hydrogenation and Oxidation Reactions, *Nano-Structures & Nano-Objects*, 18 (2019) 100287.
- [22] T.W. van Deelen, C. Hernández Mejía, K.P. de Jong, Control of Metal-Support Interactions in Heterogeneous Catalysts to Enhance Activity and Selectivity, *Nature Catalysis*, 2 (2019) 955-970.
- [23] S. Tian, W. Gong, W. Chen, N. Lin, Y. Zhu, Q. Feng, Q. Xu, Q. Fu, C. Chen, J. Luo, W. Yan, H. Zhao, D. Wang, Y. Li, Regulating the Catalytic Performance of Single-Atomic-Site Ir Catalyst for Biomass Conversion by Metal-Support Interactions, *ACS Catalysis*, 9 (2019) 5223-5230.
- [24] Y. Chen, S. Ji, C. Chen, Q. Peng, D. Wang, Y. Li, Single-Atom Catalysts: Synthetic Strategies and Electrochemical Applications, *Joule*, 2 (2018) 1242-1264.
- [25] Y. Lin, P. Liu, E. Velasco, G. Yao, Z. Tian, L. Zhang, L. Chen, Fabricating Single-Atom Catalysts from Chelating Metal in Open Frameworks, *Advanced Materials*, 31 (2019) 1808193.
- [26] Y. Zhang, L. Guo, L. Tao, Y. Lu, S. Wang, Defect-Based Single-Atom Electrocatalysts, *Small Methods*, 3 (2019) 1800406.
- [27] Y. Liu, Z. Li, Q. Yu, Y. Chen, Z. Chai, G. Zhao, S. Liu, W.-C. Cheong, Y. Pan, Q. Zhang, L. Gu, L. Zheng, Y. Wang, Y. Lu, D. Wang, C. Chen, Q. Peng, Y. Liu, L. Liu, J. Chen, Y. Li, A General Strategy for Fabricating Isolated Single Metal Atomic Site Catalysts in Y Zeolite, *Journal of the American Chemical Society*, 141 (2019) 9305-9311.
- [28] J.D. Kistler, N. Chotigkrai, P. Xu, B. Enderle, P. Praserthdam, C.-Y. Chen, N.D. Browning, B.C. Gates, A Single-Site Platinum CO Oxidation Catalyst in Zeolite KLTL: Microscopic and Spectroscopic Determination of the Locations of the Platinum Atoms, *Angewandte Chemie International Edition*, 53 (2014) 8904-8907.
- [29] F.M. Pinto, V.Y. Suzuki, R.C. Silva, F.A. La Porta, Oxygen Defects and Surface Chemistry of Reducible Oxides, *Frontiers in Materials*, 6 (2019).
- [30] X. Zhou, L. Chen, G.E. Sterbinsky, D. Mukherjee, R.R. Unocic, S.L. Tait, Pt-Ligand single-atom catalysts: tuning activity by oxide support defect density, *Catal. Sci. Technol.*, 10 (2020) 3353-3365.
- [31] T.W. Morris, I.J. Huerfano, M. Wang, D.L. Wisman, A.C. Cabelof, N.U. Din, C.D. Tempas, D. Le, A.V. Polezhaev, T.S. Rahman, K.G. Caulton, S.L. Tait, Multi-electron Reduction Capacity and Multiple Binding Pockets in Metal-Organic Redox Assembly at Surfaces, *Chem. Eur. J.*, 25 (2019) 5565-5573.
- [32] D. Skomski, C.D. Tempas, B.J. Cook, A.V. Polezhaev, K.A. Smith, K.G. Caulton, S.L. Tait, Two- and Three-Electron Oxidation of Single-Site Vanadium Centers at Surfaces by Ligand Design, *J. Am. Chem. Soc.*, 137 (2015) 7898-7902.
- [33] C.D. Tempas, Tobias W. Morris, D.L. Wisman, D. Le, N.U. Din, C.G. Williams, M. Wang, A.V. Polezhaev, T.S. Rahman, K.G. Caulton, S.L. Tait, Redox-Active Ligand Controlled Selectivity of Vanadium Oxidation on Au(100), *Chemical Science*, 9 (2018) 1674-1685.
- [34] Z. Huang, X. Gu, Q. Cao, P. Hu, J. Hao, J. Li, X. Tang, Catalytically Active Single-Atom Sites Fabricated from Silver Particles, 51 (2012) 4198-4203.
- [35] B. Qiao, A. Wang, X. Yang, L.F. Allard, Z. Jiang, Y. Cui, J. Liu, J. Li, T. Zhang, Single-Atom Catalysis of CO Oxidation Using Pt₁/FeO_x, *Nature Chemistry*, 3 (2011) 634-641.
- [36] P. Liu, Y. Zhao, R. Qin, S. Mo, G. Chen, L. Gu, D.M. Chevrier, P. Zhang, Q. Guo, D. Zang, B. Wu, G. Fu, N. Zheng, Photochemical Route for Synthesizing Atomically Dispersed Palladium Catalysts, 352 (2016) 797-800.

- [37] Z. Novotný, G. Argentero, Z. Wang, M. Schmid, U. Diebold, G.S. Parkinson, Ordered Array of Single Adatoms with Remarkable Thermal Stability, *Physical Review Letters*, 108 (2012) 216103.
- [38] X. Zhou, G.E. Sterbinsky, E. Wasim, L. Chen, S.L. Tait, Tuning Ligand-Coordinated Single Metal Atoms on TiO₂ and their Dynamic Response during Hydrogenation Catalysis, *ChemSusChem*, 14 (2021) 3825-3837.
- [39] L. Chen, I.S. Ali, G.E. Sterbinsky, J.T.L. Gamler, S.E. Skrabalak, S.L. Tait, Alkene Hydrosilylation on Oxide-Supported Pt-Ligand Single-Site Catalysts, *ChemCatChem*, 11 (2019) 2843-2854.
- [40] L. Chen, G.E. Sterbinsky, S.L. Tait, Synthesis of platinum single-site centers through metal-ligand self-assembly on powdered metal oxide supports, *J. Catal.*, 365 (2018) 303-312.
- [41] N. Kumaresan, K. Ramamurthi, Synthesis of ZnO/rGO Nanocomposites by Wet Impregnation Method for Photocatalytic Performance Against RhB dye and 4-chlorophenol Under UV Light Irradiation, *Journal of Materials Science: Materials in Electronics*, 31 (2020) 3361-3374.
- [42] G. Kresse, J. Furthmüller, Efficiency of Ab-Initio Total Energy Calculations for Metals and Semiconductors Using a Plane-Wave Basis Set, *Computational Materials Science*, 6 (1996) 15-50.
- [43] G. Kresse, J. Hafner, Ab Initio Molecular Dynamics for Liquid Metals, *Physical Review B*, 47 (1993) 558.
- [44] G. Kresse, D. Joubert, From Ultrasoft Pseudopotentials to the Projector Augmented-Wave Method, *Physical Review B*, 59 (1999) 1758.
- [45] P.E. Blöchl, Projector augmented-wave method, *Physical Review B*, 50 (1994) 17953.
- [46] J.P. Perdew, K. Burke, M. Ernzerhof, Generalized Gradient Approximation Made Simple, *Physical Review Letters*, 77 (1996) 3865.
- [47] S. Grimme, J. Antony, S. Ehrlich, H. Krieg, A Consistent and Accurate Ab Initio Parametrization of Density Functional Dispersion Correction (DFT-D) for the 94 Elements H-Pu, *The Journal of Chemical Physics*, 132 (2010) 154104.
- [48] S. Dudarev, G. Botton, S. Savrasov, C. Humphreys, A. Sutton, Electron-Energy-Loss Spectra and the Structural Stability of Nickel Oxide: An LSDA+ U study, *Physical Review B*, 57 (1998) 1505–1509.
- [49] J.J. Plata, A.M. Márquez, J.F. Sanz, Communication: Improving the Density Functional Theory+U description of CeO₂ by Including the Contribution of the O 2p Electrons, *The Journal of Chemical Physics*, 136 (2012) 041101.
- [50] J.P. Mathew, M. Srinivasan, Photoelectron Spectroscopy (XPS) Studies on Some Palladium Catalysts, *European Polymer Journal*, 31 (1995) 835-839.
- [51] L. Chen, A. Yelon, E. Sacher, X-ray Photoelectron Spectroscopic Studies of Pd Nanoparticles Deposited onto Highly Oriented Pyrolytic Graphite: Interfacial Interaction, Spectral Asymmetry, and Size Determination, *The Journal of Physical Chemistry C*, 115 (2011) 7896-7905.
- [52] S.E. Stein, Infrared Spectra, in: *NIST Chemistry WebBook*, NIST Standard Reference National Institute of Standards and Technology, Gaithersburg, MD, 2003.
- [53] M. Muir, M. Trenary, Adsorption of CO to Characterize the Structure of a Pd/Ag(111) Single-Atom Alloy Surface, *The Journal of Physical Chemistry C*, 124 (2020) 14722-14729.
- [54] J. Moon, Y. Cheng, L.L. Daemen, M. Li, F. Polo-Garzon, A.J. Ramirez-Cuesta, Z. Wu, Discriminating the Role of Surface Hydride and Hydroxyl for Acetylene Semihydrogenation over Ceria through In Situ Neutron and Infrared Spectroscopy, *ACS Catalysis*, 10 (2020) 5278-5287.